Mon. Not. R. Astron. Soc. **308**, 54–66 (1999)

One-dimensional electric field structure of an outer gap accelerator – I. γ-ray production resulting from curvature radiation

K. Hirotani[1]★ and S. Shibata[2]

[1]*National Astronomical Observatory, Osawa, Mitaka, Tokyo 181-8588, Japan*
[2]*Department of Physics, Yamagata University, Yamagata 990-8560, Japan*

Accepted 1999 March 26. Received 1999 March 26; in original form 1998 February 23

ABSTRACT

We study the structure of a stationary and axisymmetric charge-deficient region (or potential gap) in the outer magnetosphere of a spinning neutron star. Assuming the existence of global current flow patterns in the magnetosphere, the charge depletion causes a large electric field along the magnetic field lines. This longitudinal electric field accelerates migratory electrons and/or positrons to ultrarelativistic energies. These relativistic electrons/positrons radiate γ-ray photons by curvature radiation. These γ-rays, in turn, produce yet more radiating particles by colliding with ambient X-ray photons, leading to a pair production cascade in the gap. The replenished charges partially screen the longitudinal electric field, which is self-consistently solved together with the distribution of $e^{\pm}$ and γ-ray photons. We find the voltage drop in the gap as a function of the soft photon luminosity. It is demonstrated that the voltage drop is less than 3×10^{13} V when the background X-ray radiation is as luminous as Vela. However, this value increases with decreasing X-ray luminosity and attains 3×10^{15} V when the X-ray luminosity is as low as $L_{\rm X}=10^{31}\,{\rm erg\,s^{-1}}$.

Key words: magnetic fields – pulsars: general – gamma-rays: theory.

1 INTRODUCTION

In the past 20 years there has been increasing interest in the study of high-energy emission from the pulsar magnetosphere. Attempts to model the production of high-energy radiation have concentrated on two scenarios: polar cap models with emission altitudes of $\sim10^4$ cm to several neutron star radii over a pulsar polar cap surface (Harding, Tademaru & Esposito 1978; Daugherty & Harding 1982, 1996; Dermer & Sturner 1994; Sturner, Dermer & Michel 1995; also see Scharlemann, Arons & Fawley 1978 for the slot gap model) and outer gap models with acceleration occurring in the open field zone located near the light cylinder (Chen, Ho & Ruderman 1986a,b, hereafter CHR; Chiang & Romani 1992, 1994; Romani 1996). Both of these pictures have had some success in reproducing global properties of the observed emission. However, there is an important difference between these two models. A polar gap accelerator releases very little angular momentum, while an outer gap one could radiate angular momentum efficiently. More specifically, the total angular momentum loss rate must equal the energy loss rate divided by the angular velocity of the star, implying an average location of energy loss on the light cylinder (Cohen & Treves 1972; Holloway 1977; Shibata 1995) with distance from the rotation axis given by

$$r_{\rm LC}=\frac{c}{\Omega}=10^{8.5}\Omega_2^{-1}\,{\rm cm}, \tag{1}$$

where Ω_2 denotes the angular frequency of the neutron star, Ω, in units of $10^2\,{\rm rad\,s^{-1}}$, and c denotes the speed of light.

In the aligned models, an electron convection current is pictured as flowing out from the polar regions, crossing the field lines beyond the light cylinder, and returning to the star at lower latitudes in the poloidal plane (Fig. 1). The poloidal current is dissipation-free well within the light cylinder; however, it is likely to become dissipative beyond the light cylinder (Mestel & Shibata 1994). In any case, the argument on angular momentum loss tells us that most of the energy and angular momentum are released beyond the light cylinder; the particle acceleration (pulsar wind formation) and photon emission take place mainly beyond the light cylinder (Shibata 1995). As a result, the poloidal current circuit closes beyond the light cylinder (Fig. 1). The steady spin-down of the star is, therefore, linked to the problem of the returning current.

On these grounds, the purpose here is to explore a little further into a model of an outer gap, which is located near the light cylinder. If the outer magnetosphere is filled with a plasma so that the space charge density $\rho_{\rm e}$ is equal to the Goldreich–Julian density [$\rho_{\rm GJ}\equiv\Omega B_z/(2\pi c)$ in the non-relativistic limit], then the field-aligned electric field vanishes, where B_z is the component of the magnetic field along the rotational axis. However, the depletion of charge in the Goldreich–Julian model in a region

★ E-mail: hirotani@hotaka.mtk.nao.ac.jp

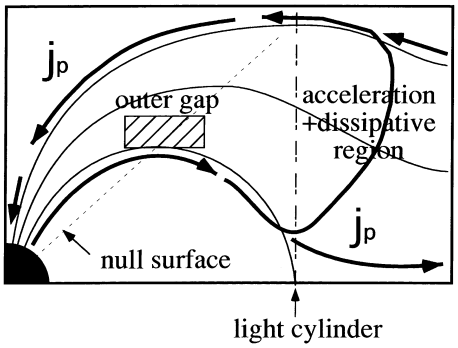

Figure 1. A schematic figure (side view) of a global current flow in the magnetosphere of an aligned rotator.

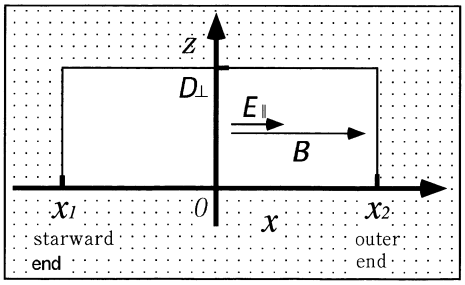

Figure 2. Rectilinear approximation of the outer gap. The null surface is approximated by the z-axis ($x = 0$). The y-axis, which designates azimuth, is not depicted, to avoid complication.

where it could not be resupplied may cause a vacuum region to develop. Holloway (1973) pointed out the possibility that a region that lacks plasma is formed around the surface on which ρ_{GJ} changes its sign.

CHR developed a version of an outer magnetospheric γ-ray emission zone in which acceleration in the Holloway gaps above the null surface brought particles to large Lorentz factors ($\sim 10^{7.5}$). These primary charges produce high-energy γ-ray photons, some (or most) of which collide with soft photons to materialize as secondary pairs. The resulting secondary charges suffer strong synchrotron losses to emit secondary radiation. The secondary photons, in turn, materialize as low-energy tertiary pairs, which were argued to produce the soft tertiary photon bath needed for the original gap closure.

However, no study has ever tried to reveal the spatial structure of the acceleration field consistently with the plasma distributions. CHR assumed a uniform potential drop (or used a particular solution of the vacuum Poisson equation), so that the acceleration field was $\sim V_{gap}/r_{LC}$, where V_{gap} is the voltage drop in the gap. Subsequently, Romani (1996) assumed its functional form as $\sim r^{-1}$ in the outer gap and computed γ-ray pulse profiles and spectra. In polar cap models, on the other hand, Michel (1991, 1993) investigated the formation of dense charged bunches that can produce coherence at radio frequencies, and analysed the time development of pair-production discharges assuming a uniform acceleration field.

In this paper, we explicitly solve the spatial distribution of $E_{\parallel}$ together with those of particles ($e^{\pm}$) and γ-ray distribution functions, by solving the Poisson equation and the Boltzmann equations of $e^{\pm}$ and γ-ray photons self-consistently. This method was originally examined by Beskin, Istomin & Par'ev (1992) and developed more quantitatively by Hirotani & Okamoto (1998) in the investigation of a pair production cascade in a black hole magnetosphere. In this work, γ-ray photons are supposed to be produced by curvature radiation, and particles by photon–photon pair production. For simplicity, we assume an aligned rotator, the rotational axis of which is parallel to the magnetic dipole moment, before analysing the more difficult but realistic problem of oblique rotators. For such an aligned rotator, $\rho_{GJ} < 0$ on the polar side of the null surface, on which ρ_{GJ} vanishes, and $\rho_{GJ} > 0$ on the equatorial side.

For simplicity and for ease of specifying some parameters, we assume axisymmetry. In the previous paragraphs, a model with a current circuit running through the outer gap has been outlined during use of the axisymmetric model by Mestel & Shibata (1994). However, some authors think that aligned rotators are inactive with a static electrosphere (Michel 1998), and this issue is controversial. In any case, the present model is generic in the sense that what we consider is the dynamics around the null surface when the current pierces through it; therefore, the result is applicable to oblique rotators.

In the next section, we discuss the physical processes of pair production cascades in the outer magnetosphere of a pulsar and present basic equations describing the system. We then solve these equations in Section 3 and reveal the quantitative characteristics of pair production cascades. In the final section, we point out essential differences of our model from CHR and discuss the validity of the assumptions made in this paper.

2 PAIR PRODUCTION CASCADE IN THE OUTER GAP

We first reduce the Poisson equation into a one-dimensional form in Section 2.1. Next, we present a one-dimensional description of $e^{\pm}$ number densities in Section 2.2, and introduce a 'grey' approximation for the γ-ray distribution in Section 2.3.

2.1 Reduction of the Poisson equation

To simplify the geometry, let us introduce a rectilinear approximation for a region around the null surface. Suppose that the magnetic field lines are the straight lines parallel to the x-axis (Fig. 2). x is an outwardly increasing coordinate along a magnetic field line, while y designates azimuth. We approximate the null surface by the z-axis ($x = 0$). The y-dependence does not appear under the assumption of axisymmetry. By using this rectilinear coordinate, the Poisson equation for the non-corotating electric potential, Φ, becomes

$$-\left(\frac{\partial^2}{\partial x^2}+\frac{\partial^2}{\partial z^2}\right)\Phi(x,z) = 4\pi[e(N_+ - N_-) - \rho_{GJ}], \qquad (2)$$

where N_+ and N_- refer to the spatial number densities of e^+ and e^-, respectively; e refers to the magnitude of the charge on the electron.

If the transfield thickness of the gap, $D_\perp$, is sufficiently large compared with the longitudinal thickness of the gap, H, then we can neglect the z-dependence of quantities, that is $\partial^2/\partial z^2 = 0$. As will be shown later, however, $D_\perp$, which is determined by quantum electrodynamic processes, can be as large as the longitudinal thickness. To consider these effects, we use an approximation $\partial^2\Phi/\partial z^2 = -\Phi/D_\perp^2$ (Michel 1974). This approximation stands for the fact that the accelerating region is bounded on $z = 0$ and $z = D_\perp$ by the side walls on which Φ and hence $E_{\parallel}$ vanish.

For the first-order approximation, the primary effect of field line curvature appears in the x-dependence of $\rho_{\rm GJ}$. Therefore, we adopt the Taylor expansion around the null surface, although we are still in rectilinear coordinates. Thus we arrive at the following Poisson equation in the first-order approximation:

$$-\frac{{\rm d}^2\Phi}{{\rm d}x^2} = -\frac{\Phi}{D_\perp^2} + 4\pi[e(N_+ - N_-) - \left(\frac{\partial\rho_{\rm GJ}}{\partial x}\right)_0 x], \tag{3}$$

where the expansion coefficient of $\rho_{\rm GJ}$ is evaluated at $x = 0$.

2.2 One-dimensional description of the particle distribution

The number densities of individual particle species, $N_\pm$, follow one-dimensional continuity equations with a source term that is caused by the photon–photon pair production process. The most effective assumption for the particle motion in the gap arises from the fact that the velocity saturates immediately after their birth, in the balance between the radiation reaction force and the electric force. The reaction force is mainly caused by curvature radiation if the gap is embedded in a moderate X-ray photon field, the energy density of which satisfies $U_{\rm X} < 10^6\,{\rm erg\,cm^{-3}}$, such as those of Vela, B1706-44, B1055-52 and Geminga. For higher photon densities, such as for the Crab pulsar, the inverse Compton process becomes the dominant process. We investigate such cases in another paper (Hirotani & Shibata 1999, hereafter Paper II). If we evaluate $U_{\rm X}$ at the radius $r = 0.67r_{\rm LC}$, which is the intersection of the null surface and the last open field line for an aligned rotator (Fig. 3), and hence a presumed central region of the outer gap, we obtain

$$U_{\rm X} = L_{\rm X}/[4\pi(0.67r_{\rm LC})^2c] = 6.0\times10^4 L_{33}\Omega_2^2\,{\rm erg\,cm^{-3}}, \tag{4}$$

where $L_{33} \equiv L_{\rm X}/(10^{33}\,{\rm erg\,s^{-1}})$ is a dimensionless X-ray luminosity, $L_{\rm X}$.

Equating the electric force $e|{\rm d}\Phi/{\rm d}x|$ and the radiation reaction force, we obtain the saturated Lorentz factor at each point as follows:

$$\Gamma = \left(\frac{3R_{\rm c}^2}{2e}|\frac{{\rm d}\Phi}{{\rm d}x}| + 10^{24}\right)^{1/4}, \tag{5}$$

where $R_{\rm c}$ is the radius of curvature. The term 10^{24} is added in the parenthesis for a realistic treatment of the boundaries of the gap. Near the boundaries, where the diminished electric field no longer contributes to the force balance, the particles move almost freely with $\Gamma \sim 10^{24}/10^4 = 10^6$ with a modest radiation reaction, the damping length of which is larger than the width of the boundary layer.

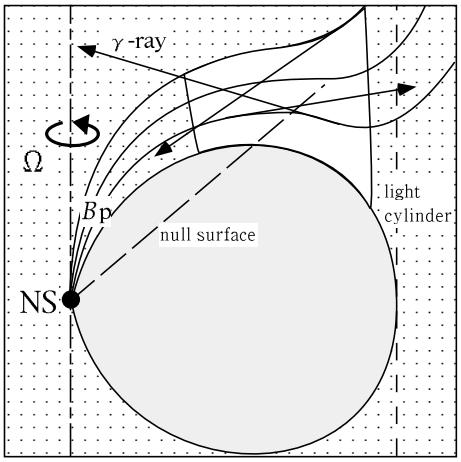

Figure 3. A side view of a hypothetical outer magnetospheric gap in which a pair production cascade takes place. γ-ray photons are produced by curvature radiation. Their initial momentum is along the local poloidal magnetic field line, and deviates as they propagate.

As will be shown in Section 5, the pitch angles of particles are essentially zero, because of $E_\parallel$ acceleration. Therefore, the longitudinal velocities of particles become virtually $\pm c$. This simplifies the continuity equations of $e^\pm$s significantly. Without loss of any generality, we can assume that the electric field is positive in the gap, in which e^+s (or e^-s) move outwards (or inwards). In the rectilinear coordinate, their continuity equations then become

$$+c\frac{{\rm d}N_+}{{\rm d}x} = \int_{-\infty}^{\infty}{\rm d}k_\gamma\eta_{\rm p}(|k_\gamma|)G(x,k_\gamma), \tag{6}$$

$$-c\frac{{\rm d}N_-}{{\rm d}x} = \int_{-\infty}^{\infty}{\rm d}k_\gamma\eta_{\rm p}(|k_\gamma|)G(x,k_\gamma), \tag{7}$$

where G refers to the distribution function of γ-ray photons having momentum k_γ along the x-coordinate. The angle-averaged pair production redistribution function $\eta_{\rm p}$ is defined by (Berestetskii, Lifshitz & Pitaevskii 1989)

$$\eta_{\rm p}(|k_\gamma|) = \frac{c}{2}\int_{-1}^{1}{\rm d}\mu\int_{2m_{\rm e}c/(1-\mu)k_\gamma}^{\epsilon_{\rm X}^{\rm max}}{\rm d}\epsilon_{\rm X}\frac{{\rm d}N_{\rm X}}{{\rm d}\epsilon_{\rm X}}\sigma_{\rm p}(v), \tag{8}$$

$$\sigma_{\rm p}(v) \equiv \frac{3}{16}\sigma_{\rm T}(1-v^2)\left[(3-v^4)\ln\frac{1+v}{1-v} - 2v(2-v^2)\right], \tag{9}$$

$$v(|k_\gamma|,\epsilon_{\rm X},\mu) \equiv \sqrt{1-\frac{2}{1-\mu}\frac{m_{\rm e}c}{|k_\gamma|\epsilon_{\rm X}}}, \tag{10}$$

where ${\rm d}N_{\rm X}$ is the number density of X-ray photons in the energy interval between $m_{\rm e}c^2\epsilon_{\rm X}$ and $m_{\rm e}c^2(\epsilon_{\rm X}+{\rm d}\epsilon_{\rm X})$; μ is the cosine of the colliding angle of the soft and the hard photons. The upper cut-off energy of the X-ray field is designated as $m_{\rm e}c^2\epsilon_{\rm X}^{\rm max}$.

2.3 Grey approximation

Let us turn to the discussion on γ-ray distribution functions. The spectrum of curvature of γ-ray photons peaks near the frequency $0.5\nu_{\rm c} = 3\Gamma^3c/(8\pi R_{\rm c})$, where $R_{\rm c}$ is the curvature radius of the field line. As we shall see in Section 4.1, $\Gamma \sim 10^{7.4}$ holds in the gap; therefore, we obtain $0.5h\nu_{\rm c} \approx 3\,{\rm GeV}$. On the other hand, sub-GeV curvature photons scarcely pair produce on a sub-keV background. Therefore, most of the γ-ray photons that can materialize are distributed in a relatively limited energy range of several GeV. On these grounds, we adopt a 'grey' approximation instead of considering a detailed γ-ray spectrum in this paper. Such a simplified treatment will not be allowed if we consider inverse Compton scatterings as a γ-ray production process.

First, we derive the continuity equations of γ-ray photons. In the rectilinear approximation, γ-ray photons are considered to be directed only in the $\pm x$ direction, which coincides with the direction of their initial momenta. In other words, their momentum k_γ equals $|k_\gamma|$ for outwardly propagating γ-ray photons while it equals $-|k_\gamma|$ for inwardly propagating ones. In general, their propagation direction deviates, however, from the curved field lines (Fig. 3). Nevertheless, the pair production rate, which essentially governs the gap structure, does not depend on the γ-ray propagation direction, provided that the background

radiation field is isotropic. In the present paper, we thus neglect minor details about transfield components of γ-ray momenta and approximate the γ-ray continuity equations by the one-dimensional form (see Appendix)

$$\frac{\mathrm{d}G_+}{\mathrm{d}x} = -\langle\eta_\mathrm{p}\rangle G_+ + \frac{16\pi e^2}{9hR_\mathrm{C}}\Gamma N_+, \tag{11}$$

$$\frac{\mathrm{d}G_-}{\mathrm{d}x} = \langle\eta_\mathrm{p}\rangle G_- - \frac{16\pi e^2}{9hR_\mathrm{C}}\Gamma N_-. \tag{12}$$

Secondly, in accordance with the introduction of the grey approximation, let us rewrite the particle continuity equations (6) and (7) in the following forms:

$$c\frac{\mathrm{d}N_+}{\mathrm{d}x} = \langle\eta_\mathrm{p}\rangle[G_+(x) + G_-(x)], \tag{13}$$

$$c\frac{\mathrm{d}N_-}{\mathrm{d}x} = -\langle\eta_\mathrm{p}\rangle[G_+(x) + G_-(x)]. \tag{14}$$

The migrating $\mathrm{e}^\pm$s and the γ-ray photons in the gap are described by differential (3) and (11)–(14).

3 DIMENSIONLESS FORMULATION

To show that the system is described by a few parameters that have reasonable meanings, we non-dimensionalize the basic equations in Section 3.1 and present suitable boundary conditions in Section 3.2.

3.1 Dimensionless basic equations

In the potential gap, a characteristic length-scale in $E_\parallel$ acceleration is c/ω_p, where the plasma frequency ω_p is defined by

$$\omega_\mathrm{p} = \sqrt{\frac{4\pi e^2}{m_\mathrm{e}}\frac{\Omega B}{2\pi ce}} = 1.875\times10^7\Omega_2^{1/2}B_5^{1/2} > \mathrm{rad\,s^{-1}}, \tag{15}$$

where $\Omega_2 \equiv \Omega/(10^2\,\mathrm{rad\,s^{-1}})$. Evaluating B at the null surface of an aligned rotator, we obtain

$$B_5 \equiv \frac{B}{10^5\,\mathrm{G}} = 1.76\mu_{30}\Omega_2^2, \tag{16}$$

where μ_{30} is the nondimensional dipole moment in units of $10^{30}\,\mathrm{G\,cm^3}$. The length-scale c/ω_p characterizes the thickness of the boundary layers where $E_\parallel$ vanishes and the wavelength of excited waves. There is, indeed, another characteritic length-scale, the pair production mean free path, λ_p. However, λ_p depends on the photon field and the pair production processes under consideration. Therefore, we normalize the length-scales by c/ω_p in this paper, leaving room for future investigation of the boundary layers and wave excitation.

First, introducing the following two dmensionless quantities,

$$\xi \equiv \frac{\omega_\mathrm{p}}{c}x = 6.25\times10^{-4}\Omega_2^{1/2}B_5^{1/2}x \tag{17}$$

and

$$\Delta_\perp \equiv \frac{\omega_\mathrm{p}}{c}D_\perp, \tag{18}$$

and assuming an aligned rotator, we can simplify the Poisson equation (3) to the form

$$E_\parallel = -\frac{\mathrm{d}\varphi}{\mathrm{d}\xi} \tag{19}$$

and

$$\frac{\mathrm{d}E_\parallel}{\mathrm{d}\xi} = -\frac{\varphi}{\Delta_\perp^2} + n_+(\xi) - n_-(\xi) - A\xi, \tag{20}$$

where the dimensionless electrostatic potential and electric field are defined by

$$\varphi(\xi) \equiv \frac{e\Phi(x)}{m_\mathrm{e}c^2}, \tag{21}$$

$$E_\parallel \equiv -\frac{\mathrm{d}\varphi}{\mathrm{d}\xi} = \frac{e(-\mathrm{d}\Phi/\mathrm{d}x)}{m_\mathrm{e}c\omega_\mathrm{p}} \tag{22}$$

$$= 3.12\times10^{-5}\left(\frac{-\mathrm{d}\Phi/\mathrm{d}x}{\mathrm{V/m}}\right)\frac{1}{\sqrt{\Omega_2 B_5}}, \tag{23}$$

and the particle densities are normalized in terms of the Goldreich–Julian density

$$n_\pm(\xi) \equiv \frac{2\pi ce}{\Omega B}N_\pm(x); \tag{24}$$

moreover, A is the dimensionless expansion coefficient of ρ_GJ at the null surface. The value of A can be estimated as

$$A \equiv \frac{c}{\omega_\mathrm{p}}\frac{2\pi c}{\Omega B}\left(\frac{\partial\rho_\mathrm{GJ}}{\partial x}\right)_0 \approx \frac{c}{\omega_\mathrm{p}R_\mathrm{c}}$$

$$= 1.1\times10^{-5}\Omega_2^{1/2}B_5^{-1/2}\left(\frac{R_\mathrm{c}}{0.5r_\mathrm{LC}}\right)^{-1}. \tag{25}$$

Here, $R_\mathrm{C} = 0.5r_\mathrm{LC}$ gives a good estimate.

Secondly, we can rewrite the continuity equations of particles (13) and (14) as

$$\frac{\mathrm{d}n_+}{\mathrm{d}\xi} = \hat{\eta}_\mathrm{p}[g_+(\xi) + g_-(\xi)], \tag{26}$$

$$\frac{\mathrm{d}n_-}{\mathrm{d}\xi} = -\hat{\eta}_\mathrm{p}[g_+(\xi) + g_-(\xi)], \tag{27}$$

where

$$\hat{\eta}_\mathrm{p} \equiv \langle\eta_\mathrm{p}\rangle/\omega_\mathrm{p} \approx \frac{c}{\omega_\mathrm{p}}\times0.2\sigma_\mathrm{T}\times N_\mathrm{X}$$

$$= 2.2\times10^{-8}L_{33}\Omega_2^{3/2}B_5^{-1/2}\left(\frac{m_\mathrm{e}c^2\epsilon_\mathrm{X}}{0.4\,\mathrm{keV}}\right)^{-1}; \tag{28}$$

the γ-ray spatial number densities are normalized in the same way as $n_\pm$,

$$g_+(\xi) \equiv \frac{2\pi ce}{\Omega B}G_+(x), \tag{29}$$

$$g_-(\xi) \equiv \frac{2\pi ce}{\Omega B}G_-(x). \tag{30}$$

We implicitly assumed here that the soft photons are supplied by the surface blackbody radiation of temperature $kT \sim 0.15\,\mathrm{keV}$, which is applicable for Vela, B1055-52 and Geminga. A combination of equations (26) and (27) gives the current conservation law,

$$j_0 \equiv n_+(\xi) + n_-(\xi). \tag{31}$$

Here, $j_0 = 1.0$ indicates that the current density is equal to a typical Goldreich–Julian current density, $\Omega B/(2\pi)$.

Thirdly and finally, the γ-ray continuity equations (11) and (12)

become

$$\frac{\mathrm{d}g_+}{\mathrm{d}\xi} = -\hat{\eta}_\mathrm{p} g_+ + \eta_\mathrm{c} n_+, \tag{32}$$

$$\frac{\mathrm{d}g_-}{\mathrm{d}\xi} = \hat{\eta}_\mathrm{p} g_- - \eta_\mathrm{c} n_-, \tag{33}$$

where

$$\eta_\mathrm{c} \equiv \frac{16\pi e^2}{9\omega_\mathrm{p} h R_\mathrm{C}}\Gamma = 4.3\times10^{-2}\,\frac{\Gamma}{10^7}\sqrt{\frac{\Omega_2}{B_5}} \tag{34}$$

denotes the number of γ-ray photons emitted by a single e^+ or e^- in the normalization length-scale c/ω_p along the field line. As η_c is much larger than $\hat{\eta}_\mathrm{p}$ for $\Gamma \gg 10$, γ-ray production resulting from curvature radiation dominates the absorption because of γ–γ collisions in the gap.

3.2 Boundary conditions

To solve the six basic equations (19), (20), (26), (27), (32) and (33), we must adopt appropriate boundary conditions. We first consider the conditions at the *inner* boundary $\xi = \xi_1$.

For one thing, the inner boundary is defined so that $E_\parallel$ vanishes there. Therefore, we have

$$E_\parallel(\xi_1) = 0. \tag{35}$$

It is noteworthy that condition (35) is consistent with the stability condition at the plasma–vacuum interface if the electrically supported magnetospheric plasma is completely charge-separated, i.e. if the plasma cloud at $\xi < \xi_1$ is composed of electrons alone (Krause-Polstorff & Michel 1985a,b). We assume that the Goldreich–Julian plasma gap boundary is stable with $E_\parallel = 0$ at the boundary, $\xi = \xi_1$.

Furthermore, we assume that the inner boundary is grounded to the star surface, that is we put

$$\varphi(\xi_1) = 0. \tag{36}$$

What is more, we impose for simplicity the condition that no γ-rays enter from the outside of the gap, that is

$$g_+(\xi_1) = 0. \tag{37}$$

One final point is that we can impose conditions on n_+ and n_-. If the negatively charged cloud at $x < x_1$ is composed of pure electrons, then there will be no positrons penetrating into the gap at $\xi = \xi_1$. Therefore, we assume

$$n_+(\xi_1) = 0, \tag{38}$$

which yields, with the help of the charge conservation law (31),

$$n_-(\xi_1) = j_0. \tag{39}$$

Let us next consider the conditions at the *outer* boundary. The outer boundary, $\xi = \xi_2$, is defined so that $E_\parallel$ vanishes again, that is

$$E_\parallel(\xi_2) = 0. \tag{40}$$

In the same manner, at $\xi = \xi_1$, we impose both

$$g_-(\xi_2) = 0 \tag{41}$$

and

$$n_-(\xi_2) = 0. \tag{42}$$

We have eight boundary conditions in total (35)–(42) for the six differential equations; thus two extra boundary conditions must be compensated for by making the positions of the boundaries ξ_1 and ξ_2 free. The two free boundaries appear because $E_\parallel = 0$ is imposed at *both* boundaries and because j_0 is externally imposed.

In summary, the gap structure is described in terms of the following five dimensionless parameters:

$$j_0 \equiv J_0/(\Omega B/2\pi), \tag{43}$$

$$\hat{\eta}_\mathrm{p} \equiv \eta_\mathrm{p}/\omega_\mathrm{p} \propto L_\mathrm{X}\Omega^{3/2}B^{-1/2}, \tag{44}$$

$$\eta_\mathrm{c}^{-1} \propto \frac{R_\mathrm{C}}{c/\omega_\mathrm{p}} \propto (R_\mathrm{C}/r_\mathrm{LC})\sqrt{B/\Omega}, \tag{45}$$

$$\Delta_\perp = D_\perp/(c/\omega_\mathrm{p}) \propto D_\perp(\Omega B)^{1/2}, \tag{46}$$

$$\frac{m_\mathrm{e}c^3}{e^2\omega_\mathrm{p}} \propto (\Omega B)^{-1/2}. \tag{47}$$

It is important that j_0 is a free parameter in this paper, because it can be determined only from a global condition on the current circuit (e.g. Shibata 1997). It is also noteworthy that the curvature parameter η_c comes into the system in two ways: one is in determining the Goldreich–Julian distribution, $A \approx (\omega_\mathrm{p}R_\mathrm{c}/c)^{-1}$ in equation (25), and the other is in the efficiency of the γ-ray production rate in equations (32) and (33). The fifth parameter, $m_\mathrm{e}c^3/(e^2\omega_\mathrm{p})$, is necessary when we compute the terminal Lorentz factor from $E_\parallel$. In other words, equation (5) gives

$$\Gamma(\xi) = \left[\frac{3}{2}\frac{m_\mathrm{p}c^3}{e^2\omega_\mathrm{p}}\left(\frac{\omega_\mathrm{p}R_\mathrm{c}}{c}\right)^2 E_\parallel(\xi) + 10^{24}\right]^{1/4}. \tag{48}$$

Γ, and hence the fifth parameter, appears only in equations (32) and (33).

The gap structure is seemingly described by the six parameters J_0, Ω, B, L_X, R_c and $D_\perp$. However, by normalizing η_p with plasma frequency, ω_p, normalizing x, R_c and $D_\perp$ with c/ω_p, and normalizing j_0, $n_\pm$ and $g_\pm$ with their Goldreich–Julian values, we can understand that the freedom reduces from six parameters to five, that is the solutions are characterized only by the five parameters (43)–(47). For example, instead of doubling L_X, we can obtain the same six equations and the same eight boundary conditions by changing $\Omega \to \sqrt{2}\Omega$ and $B \to B/\sqrt{2}$. On these grounds, we adopt these reasonable normalizations to investigate the physical properties of the gap.

4 RESULTS

In this section, we investigate how the solutions depend on j_0, $\hat{\eta}_\mathrm{p}$, $R_\mathrm{C}/(c/\omega_\mathrm{p})$, and, $\Delta_\perp$. We do not consider the dependence on the fifth parameter, $m_\mathrm{e}c^3/(e^2\omega_\mathrm{p})$, to keep the normalization of $\xi/x = \omega_\mathrm{p}/c$ unchanged.

4.1 Dependence on current density

To grasp the rough features, we first show some examples of the solutions of $E_\parallel(\xi)$ for several values of the 'first' parameter j_0 (see equation 43). In Fig. 4, the dotted, solid, and dashed lines correspond to $j_0 = 0.239$, 0.1 and 0.01, respectively. Other parameters are fixed as $\Omega_2 = 1.0$, $\mu_{30} = 1.0$, $L_{33} = 1.0$,

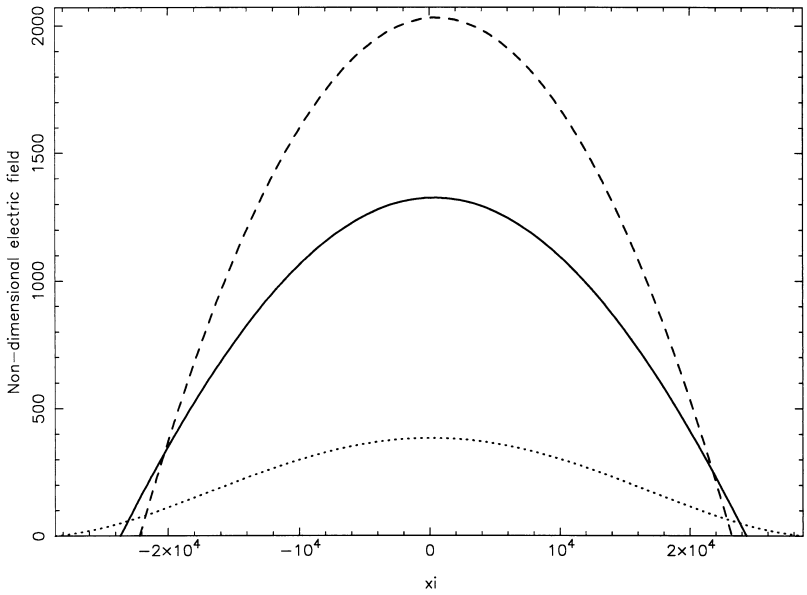

Figure 4. Examples of longitudinal electric field $E_{\parallel}(\xi)$. The dotted, solid and dashed lines represent the solutions corresponding to $j_0 = 0.239$, 0.1 and 0.01, respectively. Other parameters are fixed at $\Omega_2 = 1.0$, $\mu_{30} = 1.0$, $D_8 = 1.0$ and $L_{33} = 1.0$ throughout the gap. The real distance from the null surface is related to ξ as $x = 1.2 \times 10^3 \xi$ cm.

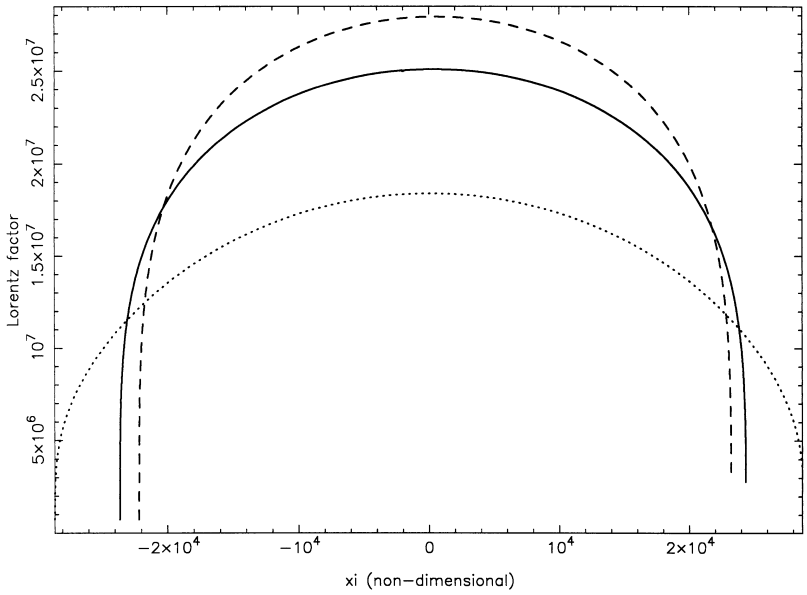

Figure 5. Examples of the Lorentz factor $\Gamma(\xi)$. The solid, dashed and dotted lines correspond to the same parameters chosen in Figs 3 and 4. $x = 1.2 \times 10^3 \xi$ cm.

$D_8 \equiv D_{\perp}/10^8\,\mathrm{cm} = 1.0$, and $R_C = 0.5 r_{LC}$, so that the remaining three parameters $\hat{\eta}_p$, $r_{LC}/(c/\omega_p)$ and $\Delta_{\perp}$ are not changed at all (see equations 44–46).

For very small j_0, the $n_+ - n_-$ term in equation (20) does not contribute. Moreover, unless the gap half-width $H/2 \approx \xi_2/2$ becomes comparable to or greater than $\Delta_{\perp} = 6.25 \times 10^4 D_8 \sqrt{\Omega_2 B_5} = 8.29 \times 10^4$, the term $-\varphi/\Delta_{\perp}^2$ is negligible. As a result, equation (20) gives approximately a quadratic solution,

$$E_{\parallel}(\xi) = E_{\parallel}(0) - (A/2)\xi^2, \tag{49}$$

which is represented by the dashed line in Fig. 4.

However, as j_0 increases, $E_{\parallel}(\xi)$ deviates from the quadratic form to have a 'brim' at the boundaries. Finally, at a certain value $j_0 = j_{cr}$, the derivative of $E_{\parallel}$ vanishes at the boundaries. In the case of $\Omega_2 = 1.0$, $\mu_{30} = 1.0$, $L_{33} = 1.0$ and $D_8 = 1.0$, j_{cr} equals 0.239, for which the solution is represented by the dotted line in Fig. 4. Above the critical current density, j_{cr}, there are no solutions satisfying the eight boundary conditions presented in Section 3.2 (see fig. 2 of Hirotani & Okamoto 1998).

It will also be useful to describe the Lorentz factor $\Gamma(\xi)$, which is related to$E_{\parallel}(\xi)$ by equation (48). The results are presented in Fig. 5; the parameters are the same as we have chosen in Fig. 4. As Fig. 5 indicates, the typical values of Γ become $10^{7.4}$ in most parts of the gap, except the case when j_0 is very close to j_{cr}. It is noteworthy that $e^{\pm}$s with $\Gamma \sim 10^{7.4}$ produce γ-ray photons of energy $\sim 0.5 h\nu_c = 3hc\Gamma^3/(8\pi R_c) \approx 3\,\mathrm{GeV}$, which most effectively collide with sub-keV photons to materialize as pairs. This result is

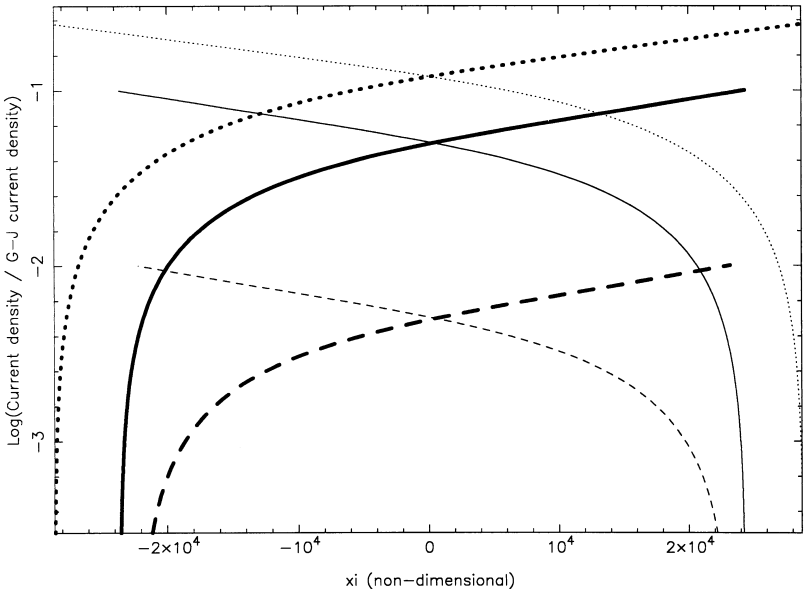

Figure 6. Examples of $\log_{10} n_+(\xi)$ (thick curves) and $\log_{10} n_-(\xi)$ (thin curves). The solid, dashed and dotted lines correspond to $j_0 = 0.1$, 0.01 and 0.239, respectively. $x = 1.2 \times 10^3 \xi$ cm.

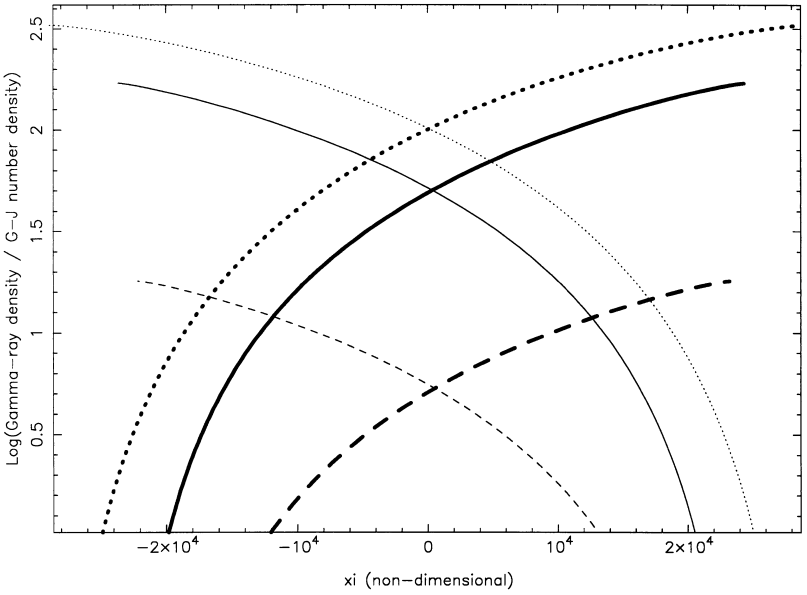

Figure 7. Examples of $\log_{10} g_+(\xi)$ (thick curves) and $\log_{10} g_-(\xi)$ (thin curves). The solid, dashed and dotted lines correspond to $j_0 = 0.1$, 0.01 and 0.239, respectively. $x = 1.2 \times 10^3 \xi$ cm.

consistent with the discussion in Section 2.3, in which we justified the grey approximation of γ-ray spectra.

Let us devote a little more space to examining particle and γ-ray fluxes. First, examples of $\log_{10} n_+$ and $\log_{10} n_-$ are shown by thick and thin curves, respectively, in Fig. 6. Parameters are chosen to be the same as in Figs 4 and 5. We can easily see that particles distribute symmetrically with respect to $\xi = 0$ in the sense that $n_+(\xi) = n_-(-\xi)$; this is because the set of equations has symmetry when the two-dimensional effect caused by the $\Delta_\perp$ term is negligible.

Secondly, examples of $\log_{10} g_+$ and $\log_{10} g_-$ are shown in Fig. 7. The thick curves denote the fluxes of g_+, while the thin curves denote those of g_-. γ-ray distribution is also symmetric with respect to $\xi = 0$. We can also see from Fig. 7 that each e^+/e^- produces $N_\gamma \equiv g_+/n_+ \sim 10^3$ γ-ray photons via curvature radiation. One of these $\sim 10^3$ γ-ray photons collides with a soft X-ray photon to materialize as a pair.

Let us briefly mention why such an active gap is maintained stationarily when a global current circuit (Fig. 1), which is closely related to the spin down of the star as described in Section 1, is realized. Seemingly, it appears as if that the discharges add negative (or positive) charges to the negative (or positive) side and act to narrow the gap to turn it off. Nevertheless, the negative charges that have migrated to the negative side of the boundary ($\xi = \xi_1$) will continue to flow toward the star by a small-amplitude residual $E_\parallel$ outside the gap, as a part of the global current system. In fact, the same number of electrons are extracted along field lines at higher latitudes to close the current circuit. In the same manner, positive charges flow outwards outside the gap. In other words, an active steady gap in which pair and γ-ray production

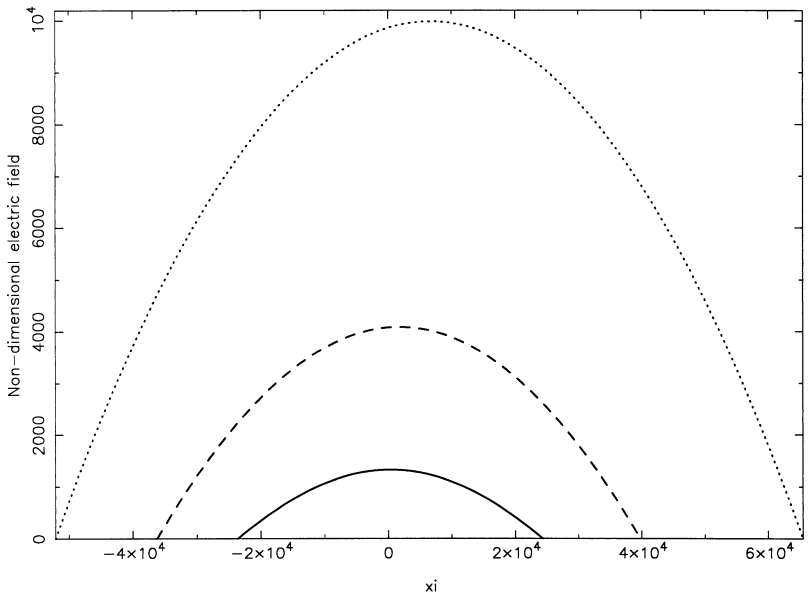

Figure 8. Longitudinal electric field $E_{\parallel}(\xi)$ in the case when $j_0 = 0.1$, $\Omega_2 = 1.0$, $\mu_{30} = 1.0$ and $D_8 = 1.0$. The solid, dashed and dotted lines represent the solutions corresponding to $L_{33} = 1.0$, 0.3 and 0.1, respectively. $x = 1.2 \times 10^3 \xi$ cm.

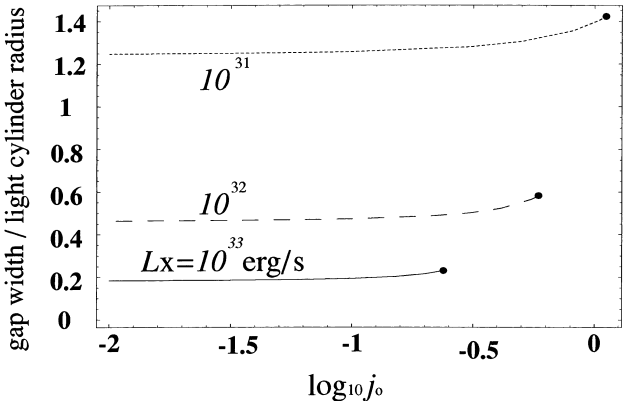

Figure 9. $H/r_{\rm LC}$ versus $\log_{10} j_0$. The solid line describes $H(j_0)$ for $L_{33} = 1.0$, while the dashed and dotted lines are for $L_{33} = 0.1$ and 0.01, respectively. The filled circle indicates the point where j_0 coincides with $j_{\rm cr}$, above which no solutions exist.

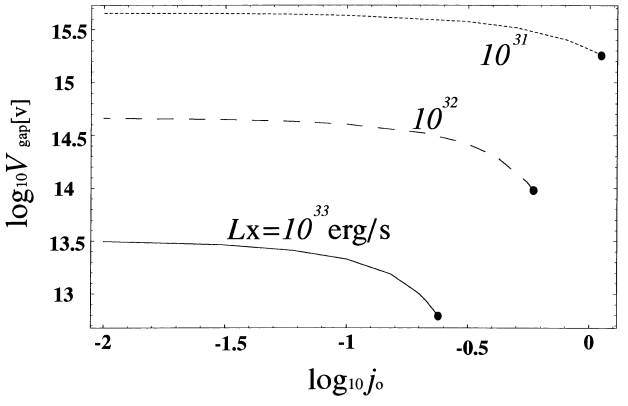

Figure 10. $\log_{10} V_{\rm gap}[V]$ vs. $\log_{10} j_0$. The solid line describes $V_{\rm gap}(j_0)$ for $L_{33} = 1.0$, while the dashed and dotted lines are for $L_{33} = 0.1$ and 0.01, respectively. The filled circle indicates the point where j_0 coincides with $j_{\rm cr}$, above which no solutions exist.

proceeds is maintained around an aligned rotator, provided that a global current circuit closes in the context of an active pulsar wind accelerator.

4.2 Dependence on the pair-production mean free path

In this subsection, we are concerned with the dependence of the solutions on the second parameter $\hat{\eta}_{\rm p} \propto L_{\rm X}$, which is inversely proportional to the pair-production mean free path. In Fig. 8 we present the solutions of $E_{\parallel}(\xi)$. The solid, dashed and dotted lines correspond to $L_{33} = 1.0$, 0.3 and 0.1, respectively. Other parameters are fixed as $j_0 = 0.1$, $\Omega_2 = 1.0$, $\mu_{30} = 1.0$, $D_8 \equiv D_{\perp}/10^8\,{\rm cm} = 1.0$ and $R_{\rm C} = 0.5 r_{\rm LC}$, so that the three parameters j_0, $r_{\rm LC}/(c/\omega_{\rm p})$ and $\Delta_{\perp}$ remain unchanged (see equations 44 and 45).

It is plain from Fig. 8 that the longitudinal electric field increases with decreasing X-ray luminosity. The reasons are twofold. First, $E_{\parallel}$ increases with increasing gap width, $H \equiv \xi_2 - \xi_1$, except when j_0 is very close to $j_{\rm cr}$, because equation (49) gives

$$E_{\parallel}(0) = \frac{AH^2}{8}. \tag{50}$$

Secondly, H increases with increasing pair-production mean free path, which is inversely proportional to the X-ray luminosity.

The results of H versus j_0 and L_{33} are summarized in Fig. 9, which displays one of the two main conclusions of this paper. The solid line indicates H versus j_0 for $L_{33} = 1.0$, while the dashed and dotted lines are for $L_{33} = 0.1$ and 0.01, respectively. Other parameters are fixed at $\Omega_2 = 1.0$ and $\mu_{30} = 1.0$. As we have discussed in the paragraph above, H increases with decreasing L_{33}. In particular, for a less luminous X-ray radiation field ($L_{33} \sim 0.01$), the gap width becomes comparable to the light cylinder radius. One may also notice that H increases with j_0. This is because $E_{\parallel}(\xi)$ has small gradients at ξ=ξ_1 and ξ_2 for large values of j_0 to form a 'brim', which enlarges the gap width to some extent.

A few further remarks should be made concerning how H is

related to $\hat{\eta}_{\rm p}$. The gap width $H \equiv \xi_2 - \xi_1$ is adjusted so that a single e^+/e^- produces copious γ-ray photons (of number N_γ) one of which materializes as a pair on average. Therefore, the probability of a γ-ray photon materializing within the gap, N_γ^{-1}, must coincide with the optical depth for absorption, $H/\lambda_{\rm p}$, where $\lambda_{\rm p} \equiv c/\hat{\eta}_{\rm p}$ is the dimensionless mean free path for pair production. Therefore, we obtain

$$H = \lambda_{\rm p}/N_\gamma. \tag{51}$$

Here, $\lambda_{\rm p}$ is inversely proportional to the X-ray luminosity (L_{33}). For example, $N_\gamma \sim n_+(\xi_2)/g_+(\xi_2) \sim 10^3$ for $L_{33} = 1.0$ and $j_0 = 0.1$ (Figs 6 and 7). In this case, equation (51) yields $H \sim 5\times10^7/10^3 \sim 5\times10^4$, which is consistent with the figures.

Equations (32) and (33) show that N_γ depends on curvature radius and the gap width in the following way:

$$N_\gamma \approx \eta_{\rm c} H \approx \frac{16\pi e^2}{9\omega_{\rm p} h R_{\rm c}}\Gamma(0) H \tag{52}$$

$$\propto \frac{16\pi e^2 H}{9\omega_{\rm p} h R_{\rm c}}\left[\frac{3}{2}\frac{m_{\rm p}c^3}{e^2\omega_{\rm p}}\left(\frac{\omega_{\rm p}R_{\rm c}}{c}\right)^2 E_\parallel(0)\right]^{1/4}. \tag{53}$$

Combining (50)–(53), we obtain

$$H \propto \hat{\eta}_{\rm p}^{-2/5}\left(\frac{\omega_{\rm p}R_{\rm c}}{c}\right)^{3/10}\left(\frac{m_{\rm p}c^3}{e^2\omega_{\rm p}}\right)^{-1/10}. \tag{54}$$

This is an analytic expression relating H and $\hat{\eta}_{\rm p}$.

Let us now develop the argument on H into how much voltage is dropped in the gap. The voltage drop, $V_{\rm gap}$, is calculated by integrating $E_\parallel$ along a field line from $\xi = \xi_1$ to ξ_2. The results are summarized in Fig. 10, which shows another main result of this paper. The solid line describes $V_{\rm gap}(j_0)$ for $L_{33} = 1.0$, while the dashed and dotted lines are for $L_{33} = 0.1$ and 0.01, respectively. Other parameters are fixed at $\Omega_2 = 1.0$ and $\mu_{30} = 1.0$.

What is most important is that $V_{\rm gap}$ is sufficiently small compared with the available electromotive force ($\sim10^{16}$ V) produced on the spinning neutron star surface when the background X-ray luminosity is as high as $L_{\rm X} = 10^{\sim32-33}\,{\rm erg\,s^{-1}}$. In other words, $V_{\rm gap}$ is less than 5×10^{14} V when $L_{\rm X}$ is greater than $10^{32}\,{\rm erg\,s^{-1}}$. However, when the X-ray luminosity is as low as $L_{\rm X} = 10^{31}\,{\rm erg\,s^{-1}}$, $V_{\rm gap}$ reaches 3×10^{15} V as a result of the large gap width, which is comparable with $r_{\rm LC}$.

The dissipated power per unit cross-section in the gap, $V_{\rm drop}\times j_0$, increases linearly with j_0 if $j_0 \ll j_{\rm cr}$. However, the power saturates at $j_0 \approx j_{\rm cr}$. For example, the power becomes $\approx1.4\times10^{16}\,{\rm W\,m^{-2}}$ at $j_0 = j_{\rm cr}$ for $L_{33} = 0.01$.

4.3 Dependence on curvature radius

In this subsection, we investigate how the gap structure depends on the curvature radius, $R_{\rm C}$, the third parameter (see equation 45). We fix all the other parameters such that $j_0 = 0.1$, and $\Omega_2 = B_5 = D_8 = L_{33} = 1.0$.

In Fig. 11, we present the results of $E_\parallel(\xi)$; the solid line corresponds to the case of $R_{\rm C} = 0.5r_{\rm LC}$, while the dashed and dotted lines correspond to $R_{\rm C} = 0.4r_{\rm LC}$ and $0.6r_{\rm LC}$, respectively. The larger the curvature radius is, the larger H becomes. This is because the increased curvature radius enables reduced γ-ray production, thereby enlarging the width of the gap in which one of the γ-ray photons materializes as a pair. However, H has realtively weak dependence on $R_{\rm c}$, because H increases by only 17 per cent from the $R_{\rm c} = 0.4r_{\rm LC}$ case to $0.6r_{\rm LC}$ one. As a result, $E_\parallel(0) \approx (A/2)H^2 \propto H^2/R_{\rm c}$ slightly increases with decreasing $R_{\rm c}$.

4.4 Dependence on transfield thickness

In the previous sections we have considered the case of $D_8 = 1.0$, which gives roughly symmetric solutions with respect to the null surface $\xi = 0$. In this subsection, we investigate the case of smaller D_8, which reduces the fourth parameter, $\Delta_\perp$ (see equation 46). In Fig. 12, we show the distribution of $E_\parallel(\xi)$. The solid, dotted and dashed lines represent the solutions corresponding to $D_8 = 1.0$, 0.3 and 0.1, respectively. Other parameters are fixed at $j_0 = 0.1$, $\Omega_2 = B_5 = L_{33} = 1.0andR_{\rm C} = 0.5r_{\rm LC}$.

For $D_8 = 0.1$, the solution is no longer symmetric and the peak shifts to the positive ξ direction. However, $V_{\rm gap}$ decreases with

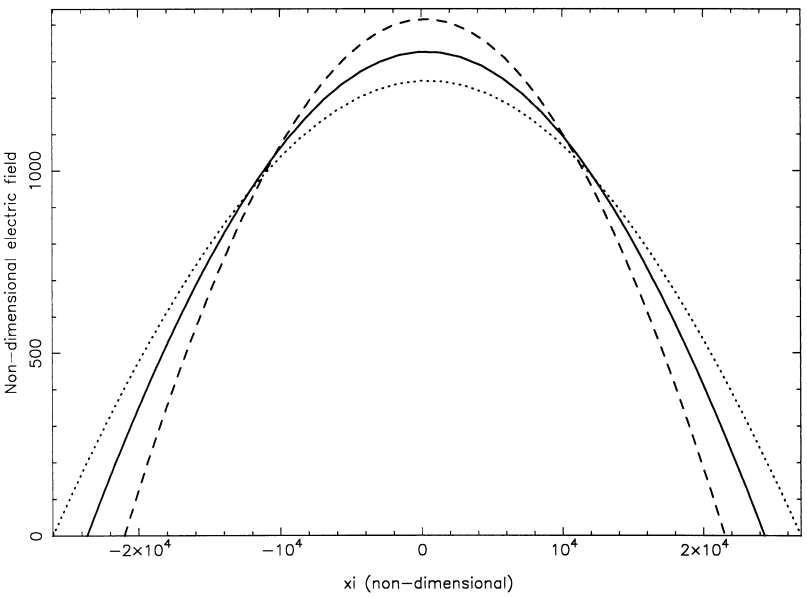

Figure 11. Longitudinal electric field $E_\parallel(\xi)$ in the case when $j_0 = 0.1$, $\Omega_2 = B_5 = D_8 = L_{33} = 1.0$. The dashed, solid and dotted lines represent the solutions corresponding to $R_{\rm C} = 0.4$, 0.5 and $0.6r_{\rm LC}$, respectively. $x = 1.2\times10^3\xi$ cm.

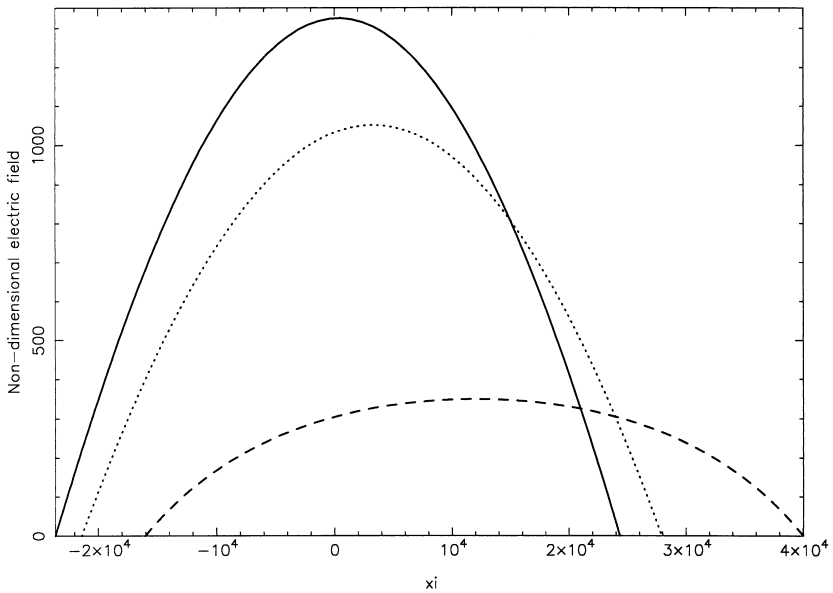

Figure 12. Longitudinal electric field $E_{\parallel}(\xi)$ in the case when $j_0 = 0.1$, $D_8 = 1.0$ and $L_{33} = 1.0$. The solid, dotted and dashed lines represent the solutions corresponding to $D_8 = 1.0$, 0.3 and 0.1, respectively. $x = 1.2 \times 10^3 \xi$ cm.

decreasing D_8. This is because $-\varphi/\Delta_\perp^2 (> 0)$ cancels the term $-A\xi$ in the region $\xi > 0$ for small $\Delta_\perp$. The reader may notice that $-\phi$ vanishes at $\xi = \xi_1$ and increases with ξ to contribute in equation (20) at larger $\xi - \xi_1$.

It is interesting to note that the gap structure qualitatively approaches that presented in CHR as $D_\perp$ decreases. In other words, the case of $D_8 = 0.1$ in Fig. 12 indicates the following two facts: (1) $E_\parallel$ becomes almost constant in the central region and (2) the gap extends from just inside the null surface to the light cylinder, owing to the existence of a wall with vanishing potential ($\Phi = 0$) in the transfield direction.

5 DISCUSSION

In summary, we have developed an one-dimensional model for an outer gap accelerator immersed in a low-luminosity X-ray field ($L_X < 10^{33}\,\mathrm{erg\,s^{-1}}$). In such a low-luminosity X-ray field, the terminal Lorentz factor exceeds 10^7; this leads to a γ-ray production via curvature radiation. Owing to the symmetric distribution of the Goldreich–Julian charge density about the null surface, the gap structure also becomes symmetric to this surface if the gap transfield thickness ($\Delta_\perp$) is greater than the longitudinal width (H). However, if $\Delta_\perp$ becomes comparable to H, the symmetry breaks down and the gap structure approaches the model of CHR(1986a,b). A typical e^+ or e^- produces 10^3 γ-ray photons that can materialize as pairs. As the background radiation field becomes less luminous, the pair-production mean free path, and hence H, increases. The most important conclusion is that the voltage drop in the gap is only 3×10^{13} V for $L_X = 10^{33}\,\mathrm{erg\,s^{-1}}$ and 3×10^{14} V for $L_X = 10^{32}\,\mathrm{erg\,s^{-1}}$. However, when the X-ray luminosity is as low as $L_X = 10^{31}\,\mathrm{erg\,s^{-1}}$, the voltage drop becomes 3×10^{15} V, which corresponds to about 30 per cent of the available EMF produced on a spinning neutron star surface, as a result of the large gap width, which is comparable with r_{LC}.

5.1 Maximum current density

Let us discuss why the maximum allowed current density, j_{cr}, is small compared with the typical Goldreich–Julian (GJ) current density, $\Omega|\boldsymbol{B}|/(2\pi e)$, where $|\boldsymbol{B}|$ refers to the absolute value of the field strength. If the local GJ charge density $\rho_{GJ} = \Omega B_z/(2\pi c)$ is filled by the charged particles produced via γ–γ collisions, the gap vanishes, or equivalently $dE_\parallel/d\xi$ and hence $E_\parallel$ vanishes. Note that $B_z/|\boldsymbol{B}|$ is small in the gap, which is located around the null surface where B_z vanishes. It follows that only a small fraction of the typical GJ current density results in $dE_\parallel/d\xi = 0$ at the boundaries of the gap. However, in this case $E_\parallel$ is not screened out in the gap, because $|n_+ - n_-| < |-A\xi|$ holds in equation (20).

The actual current density is not, however, limited by the argument above, if we release to some extent the boundary conditions (38) and (42), by which we impose no particle injection from the outside of the gap. Let us assume, for example, that some electrons are injected into the gap from the light cylinder side toward the star; we impose $n_-(\xi_2) = 0.2 j_0$, say, instead of equation (42). Then equation (31) gives $n_+(\xi_2) = 0.8 j_0$, which yields $n_+(\xi_2) - n_-(\xi_2) = 0.6 j_0$. This small factor (0.6 in this case) reduces the cancellation effect on the right-hand side of equation (20). Therefore, larger j_{cr} could be obtained if particles were injected from the outside of the gap. Such a case will be discussed in detail in a subsequent paper, in connection with a 'dead' gap in which no pair production takes place with non-vanishing $E_\parallel$.

5.2 Comparison with Chen et al.

We next discuss the essential differences from CHR. CHR hypothesized an outer gap in the region where no γ-rays penetrate. The single-signed curvature of field lines results in an exponential growth of particle number densities in the z (transfield) direction. As a result, the gap is supposed to be formed in a geometrically thin shape above the last open field lines. In another word, z dependence is essential in CHR.

On the other hand, in the present paper, it is the null surface (rather than the z dependence) that is essential for the formation of the gap. In other words, the inversion of the sign of ρ_{GJ} along the field lines leads to gap closure in the sense that $dE_\parallel/d\xi > 0$ at $\xi < 0$ and $dE_\parallel/d\xi < 0$ at $\xi > 0$. When $n_+ - n_-$ contributes in

equation (20), the basic mechanism of this $E_\parallel$ closure still works. In other words, the gap closes without the tertiary pairs, which are hypothesized in CHR, by virtue of $\rho_{\rm GJ}$ distribution. On these grounds, transfield structure does not play a primary role in the gap closure problem; therefore, we neglect such details and focus attention on the longitudinal structure of the gap in the present paper.

5.3 Validity of assumptions

First, we demonstrate that non-relativistic $e^{\pm}$s, which are turning back owing to electrostatic acceleration shortly after the birth, can be really neglected in the Poisson equations (2). Figs 4, 8, 11 and 12 indicate that $E_\parallel > 10$ holds in most parts of the gap. It follows that the turning length becomes

$$\frac{\Gamma_0 m_{\rm e} c^2}{e|{\rm d}\Phi/{\rm d}x|} \sim 10^6 \Omega_2^{-1/2} B_5^{-1/2} \left(\frac{E_\parallel}{10}\right)^{-1} \left(\frac{\Gamma_0}{10^4}\right) {\rm cm}, \tag{55}$$

which is much smaller than the gap width ($\sim 10^8$ cm). The ratio of the charge of the non-relativistic $e^{\pm}$s and that of relativistic ones is of the order of the turning length divided by the gap longitudinal width. It should therefore be concluded that the non-relativistic $e^{\pm}$s can safely be neglected in the Poisson equation.

Secondly, let us demonstrate that the the synchrotron radiation can be self-consistently neglected compared with curvature radiation in our present model. The evolution of the dimensionless momentum of a particle ($p \equiv P/m_{\rm e}c$, $|p| = \sqrt{\Gamma^2 - 1}$) and pitch angle ($\chi$) is described by

$$\frac{\rm d}{{\rm d}t}(p \sin\chi) = -\frac{1}{\tau} p^2 \sin^3\chi, \tag{56}$$

$$\frac{\rm d}{{\rm d}t}(p \cos\chi) = \frac{1}{\tau}\left[\pm f(\xi) - p^2 \sin^2\chi \cos\chi\right], \tag{57}$$

where $\tau/\Gamma \equiv 3m_{\rm e}c/(2r_0^2 B^2 \Gamma)$ expresses the synchrotron cooling time and f refers to the dimensionless electrostatic acceleration,

$$f \equiv \frac{3e}{2r_0^2 B^2} \frac{{\rm d}\Phi(x)}{{\rm d}x} = 2.7 \times 10^{10} \left(\frac{|{\rm d}\Phi/{\rm d}x|}{\rm V/m}\right) B_5^{-2}. \tag{58}$$

In equation (57), we choose the positive (or negative) sign for e^+ (or e^-). The dimensionless coordinate ξ and the time t are related by

$$\frac{{\rm d}\xi}{dt} = \omega_{\rm p} \frac{p \cos\chi}{\sqrt{1+p^2}}. \tag{59}$$

For simplicity, we assume both f and B to be constant for ξ.

As an example, we compare the trajectories of two cases: (1) $|{\rm d}\phi/{\rm d}x| = 10^3$ esu (electrostatic units) and $B = 10^5$ G, and (2) $|{\rm d}\phi/{\rm d}x| = 10^3$ esu and $B = 10^6$ G. Assuming that a pair is created at $\xi = 0$ with positive initial momenta $p = 7 \times 10^3$, we present their trajectories in Fig. 13. The ordinate expresses the longitudinal momentum, $p\cos\chi$. As can be seen from this figure, we can barely distinguish between these two cases. That is, on global scales ($|\xi| \sim 0.1 r_{\rm LC}$), there is no difference in the longitudinal motion between $B = 10^5$ G and 10^6 G cases. However, if we magnify the place of birth ($\xi = 0$), the trajectories differ between these two cases (Fig. 14). In other words, for a weak magnetic field ($B = 10^5$ G), the trajectory of a turning-back e^- becomes quadratic owing to $E_\parallel$ deceleration. However, for a strong magnetic field (B=10^6 G), it deviates from the quadratic form and turns back quickly because of synchrotron loss. In other words, it is the $E_\parallel$ acceleration that induces the pitch angle evolution in the initial stage ($t < \tau/\Gamma$) for weak B cases, while synchrotron loss contributes significantly to the evolution for strong B cases. The pitch angle evolution along the path lengths is demonstrated in Fig. 15; the ordinate is χ. It is plain from this figure that the larger B is, the faster the pitch angle evolves, as expected.

In the later stage ($t \gg \tau/\Gamma$), χ (or $\pi - \chi$) evolves as Γ_0/Γ owing to $E_\parallel$ acceleration for weak B cases, while it becomes smaller than Γ_0/Γ for strong B cases, where Γ_0 is the initial Lorentz factor (at $\xi = 0$ in this case). After the particles attain the terminal Lorentz factor, χ ceases to evolve, because synchrotron radiation does not alter χ owing to the relativistic beaming effect. As the initial $e^{\pm}$ energy, $\Gamma_0 m_{\rm e} c^2$, cannot greatly exceed several GeV, which is the typical energy of γ-ray photons radiated by $e^{\pm}$s moving along a curved field line with $\Gamma \sim 10^{7.5}$, $E_\parallel$ acceleration keeps sin χ

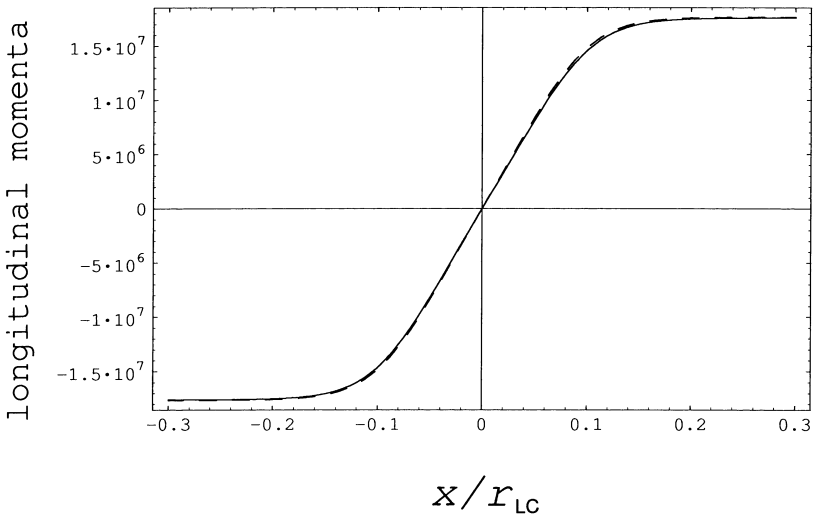

Figure 13. Trajectories of an $e^{\pm}$ pair. The abscissa is $x/r_{\rm LC}$, while the ordinate is the momentum along the field lines, $p\cos\chi$. The solid lines correspond to the trajectories of $e^{\pm}$ in the case when $B = 10^5$ G, while the dashed lines, which almost coincide with the solid ones, are for $B = 10^6$ G. Particles are assumed to be created at $x = 0$ with initial momentum $p = 7 \times 10^3$ and pitch angle $\chi = \pi/4$.

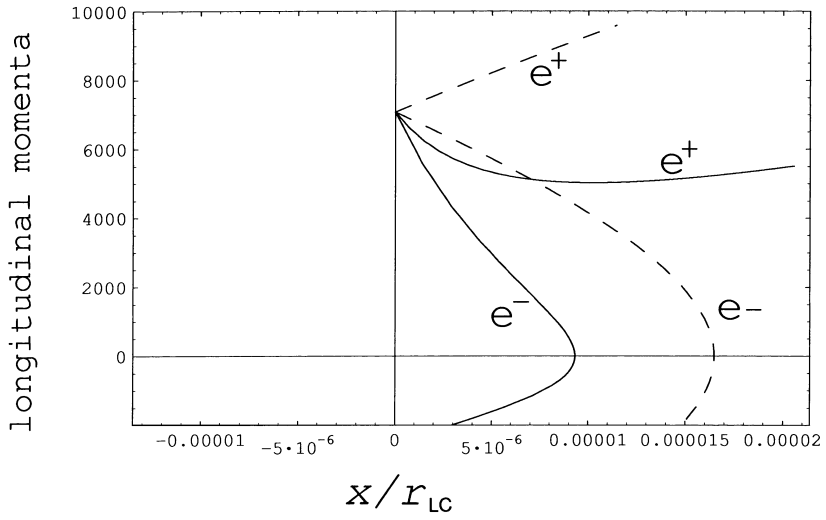

Figure 14. Magnified graph of the trajectories at the place of birth ($x = 0$). The solid lines correspond to the trajectories of $e^{\pm}$ in the case when $B = 10^5$ G, while the dashed lines are for $B = 10^6$ G.

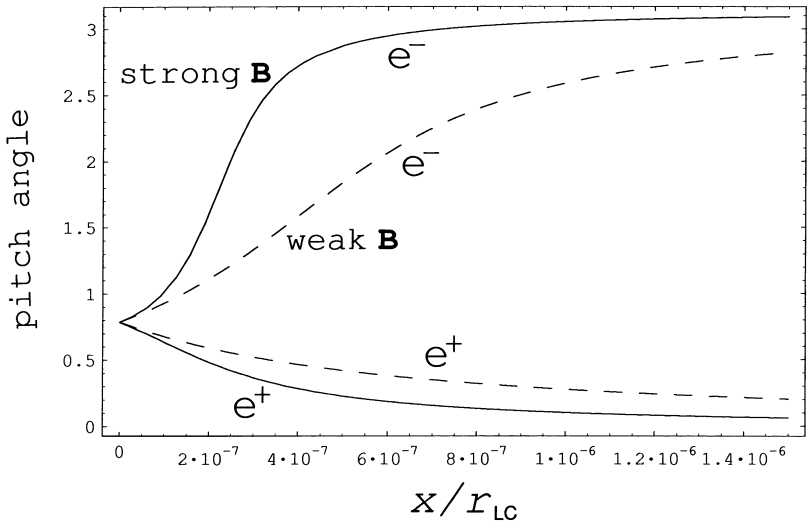

Figure 15. Pitch angle evolutions of a pair of $e^{\pm}$. The abscissa is the path length of each particle, which is magnified at the birthplace of the pair ($x = 0$).

below $\Gamma_0/\Gamma \approx 10^{-4}$. It follows that

$$\frac{P_{\rm curv}}{P_{\rm sync}} = \left(\frac{R_{\rm g}/\sin\chi}{R_{\rm c}}\right)^2 \approx 10^3 \left(\frac{\Gamma_0}{10^{3.5}}\right)^{-2} \left(\frac{\Gamma}{10^{7.5}}\right)^4 \Omega_2^2 B_5^{-2}, \qquad (60)$$

where $R_{\rm g}$ is the synchrotron gyration radius. Equation (60) indicates that the synchrotron process can be self-consistently neglected in our present model. However, this is not to deny the possibility that there exists another branch of solutions in which the synchrotron process plays a major role in γ-ray production.

Thirdly and finally, we show that inverse Compton (IC) scatterings are negligible compared with curvature radiation in γ-ray radiation in γ-ray production (or equivalently in the radiation reaction), when the X-ray radiation field is as low as $L_{\rm X} \approx 10^{31-33}\,{\rm erg\,s^{-1}}$. To see this, let us take the ratio of $P_{\rm curv}/P_{\rm IC}$, where $P_{\rm curv}/c$ and $P_{\rm IC}/c$ denote the radiation reaction forces resulting from curvature radiation and IC scatterings, respectively. By estimating the typical curvature radius of the magnetic field lines to be $0.5r_{\rm LC}$, we obtain

$$\frac{P_{\rm curv}}{c} = \frac{8e^2\Gamma^4}{3r_{\rm LC}^2} = 6.82\times10^{-36}\Omega_2^2\Gamma^4. \qquad (61)$$

The radiation reaction force resulting from IC scatterings is given by

$$\frac{P_{\rm IC}}{c} \approx cN_{\rm X}\sigma_{\rm KN}\frac{\Gamma m_{\rm e}c^2}{c} < cN_{\rm X}\sigma_{\rm T}\frac{\Gamma m_{\rm e}c^2}{c} = 8.48\times10^{-18}\Gamma\left(\frac{U_{\rm X}}{10^4\,{\rm erg\,cm^{-3}}}\right)\left(\frac{m_{\rm e}c^2\epsilon_{\rm X}}{0.4\,{\rm keV}}\right)^{-1}, \qquad (62)$$

where

$$N_{\rm X} = \frac{U_{\rm X}}{\epsilon_{\rm X}} = 1.56\times10^{13}\left(\frac{U_{\rm X}}{10^4\,{\rm erg\,cm^{-3}}}\right)\left(\frac{m_{\rm e}c^2\epsilon_{\rm X}}{0.4\,{\rm keV}}\right)^{-1}\,{\rm cm^{-3}} \qquad (63)$$

is the number density of X-ray photons evaluated at an averaged

photon energy $m_e c^2 \epsilon_X$; σ_{KN} and σ_T are the Klein–Nishina and Thomson cross-sections, respectively.

Combining the foregoing equations, we have

$$\frac{P_{curv}}{P_{IC}} > 0.804 \left(\frac{\Gamma}{10^6}\right)^3 \Omega_2^2 \left(\frac{U_X}{10^4\,\mathrm{erg\,cm^{-3}}}\right)^{-1} \left(\frac{\epsilon_X}{0.4\,\mathrm{keV}}\right). \quad (64)$$

It follows that unless $\Omega_2^2 \times (U_X/10^4\,\mathrm{erg\,cm^{-3}})^{-1}$ is much smaller than unity, the curvature drag is the force that causes the saturation of the Lorentz factor of the accelerated $e^{\pm}$s. On the other hand, if U_X is much greater than $10^4\,\mathrm{erg\,cm^{-3}}$ (as for the Crab pulsar), IC scatterings become important. These cases will be investigated in Paper II.

ACKNOWLEDGMENTS

The authors thank the Astronomical Data Analysis Center of National Astronomical Observatory, Japan, for the use of workstations. This work was supported in part by Grant-in-Aid for Scientific Research from the Ministry of Education, Science, and Culture of Japan (09680468 and 08454047).

REFERENCES

Berestetskii V. B., Lifshitz E. M., Pitaevskii L. P., 1989, Quantum Electrodynamics, 3rd edn. Nauka, Moscow
Beskin V. S., Istomin Ya N., Par'ev V. I., 1992, SvA, 36, 642
Chen K. S., Ho C., Ruderman M., 1986a, ApJ, 300, 500
Chen K. S., Ho C., Ruderman M., 1986b, ApJ, 300, 522
Chiang J., Romani R. W., 1992, ApJ, 400, 629
Chiang J., Romani R. W., 1994, ApJ, 436, 754
Cohen R. H., Treves A., 1972, A&A, 20, 305
Daugherty J. K., Harding A. K., 1982, ApJ, 252, 337
Daugherty J. K., Harding A. K., 1996, ApJ, 458, 278
Dermer C. D., Sturner S. J., 1994, ApJ, 420, L75
Harding A. K., Tademaru E., Esposito L. S., 1978, ApJ, 225, 226
Hirotani K., Okamoto I., 1998, ApJ, 497, 563
Hirotani K., Shibata S., 1999, MNRAS, 308, 67 (Paper II, this issue)
Holloway N. J., 1973, Nat, 246, 6
Holloway N. J., 1977, MNRAS, 18, 19
Krause-Polstoff J., Michel F. C., 1985a, MNRAS, 213, 43P
Krause-Polstoff J., Michel F. C., 1985b, A&A, 144, 72
Mestel L., Shibata S., 1994, MNRAS, 271, 621
Michel F. C., 1974, ApJ, 192, 713
Michel F. C., 1991, ApJ, 383, 808
Michel F. C., 1993, in Van Riper K. A., Epstein R., Ho C., eds, Proc. Los Alamos Workshop, Taos, New Mexico. Cambridge Univ. Press, Cambridge, p. 202
Michel C. F., Shibazaki N., Kawai N., Shibata S., Kifune T., 1998, Neutron Stars and Pulsars, Universal Academy Press, Tokyo, 263
Romani R. W., 1996, ApJ, 470, 469
Scharlemann E. T., Arons J., Fawley W. T., 1978, ApJ, 222, 297
Shibata S., 1995, MNRAS, 276, 537
Shibata S., 1997, MNRAS, 287, 262
Sturner S. J., Dermer C. D., Michel F. C., 1995, ApJ, 445, 736

APPENDIX A: DERIVATION OF ONE-DIMENSIONAL CONTINUITY EQUATIONS FOR γ-RAY PHOTONS

We derive equations (11) and (12) in this appendix. When γ-ray photons are produced by curvature radiation, the one-dimensional Boltzmann equations for the γ-ray photons can be written as

$$c\frac{k_\gamma}{|k_\gamma|}\frac{\partial}{\partial x}G(x,k_\gamma) = -\eta_p G(x,k_\gamma) + \frac{16\pi e^2}{9hR_C}\int_{-\infty}^{\infty} \mathrm{d}p\Gamma\delta\left(k_\gamma - \frac{3h\Gamma^3}{4\pi r_{LC}}\frac{p}{|p|}\right) \times (N_+ + N_-), \quad (A1)$$

where $G(x, k_\gamma)$ refers to the distribution function of γ-ray photons. We introduce the γ-ray production rate as the second term on the right-hand-side. In the integrand, all the γ-ray photons are assumed to be produced at $h\nu_c \approx 3\,\mathrm{GeV}$; therefore the δ-function appears.

Integrating equation (A1) over γ-ray momentum ranges of $[-\infty, 0]$ and $[0, \infty]$, we obtain

$$\frac{\mathrm{d}G_+}{\mathrm{d}x} = -\langle\eta_{p+}\rangle G_+ + \frac{16\pi e^2}{9hR_C}\Gamma N_+, \quad (A2)$$

$$\frac{\mathrm{d}G_-}{\mathrm{d}x} = \langle\eta_{p-}\rangle G_- - \frac{16\pi e^2}{9hR_C}\Gamma N_-, \quad (A3)$$

where

$$\langle\eta_{p+}\rangle \equiv \frac{\int_0^\infty \eta_p(|k_\gamma|)G(x,k_\gamma)\,\mathrm{d}k_\gamma}{\int_0^\infty G(x,k_\gamma)\,\mathrm{d}k_\gamma}, \quad (A4)$$

$$\langle\eta_{p-}\rangle \equiv \frac{\int_{-\infty}^0 \eta_p(|k_\gamma|)G(x,k_\gamma)\,\mathrm{d}k_\gamma}{\int_{-\infty}^0 G(x,k_\gamma)\,\mathrm{d}k_\gamma}; \quad (A5)$$

$G_+(x)$ and $G_-(x)$ are the spatial number density of γ-ray photons propagating outwardly and inwardly, respectively. In other words,

$$G_+(x) \equiv \int_0^\infty \mathrm{d}k_\gamma G(x,k_\gamma), \quad (A6)$$

$$G_-(x) \equiv \int_{-\infty}^0 \mathrm{d}k_\gamma G(x,k_\gamma). \quad (A7)$$

In general, the coefficients $\langle\eta_{p+}\rangle$ and $\langle\eta_{p-}\rangle$ must be solved simultaneously together with $G(x,k_\gamma)$. However, the γ-ray absorption (i.e. pair production) probability will not depend on the direction of γ-ray photons for an isotropic soft photon bath. We thus assume $\langle\eta_{p+}\rangle = \langle\eta_{p-}\rangle = \langle\eta_p\rangle \approx 0.2\sigma_T N_X c$, which yields equations (11) and (12).

This paper has been typeset from a TEX/LATEX file prepared by the author.